

# Selectivity of TiO<sub>x</sub>-Based Electron-Selective Contacts on n-Type Crystalline Silicon and Solar Cell Efficiency Potential

Valeriya Titova\* and Jan Schmidt

The selectivity parameter  $S_{10}$  of titanium oxide (TiO<sub>x</sub>)-based selective contacts on n-type silicon is experimentally extracted through measurements of the specific contact resistivity  $\rho_c$  and the recombination current density prefactor  $J_0$ , both parameters measured on fully Al-metallized samples. The contact resistivity  $\rho_c$  is determined applying the Cox and Strack method and the  $J_0$  values are extracted using dynamic infrared lifetime mapping, allowing for contactless lifetime measurements on fully metallized silicon samples in contrast to conventionally applied lifetime measurement techniques. The highest selectivity after annealing of an n-Si/SiO<sub>y</sub>/TiO<sub>x</sub>/Al contact is determined to be  $S_{10} = 11.6$ , which corresponds to a maximum achievable efficiency of 24.1% for this type of electron-selective contact. The maximum selectivity is achieved after low-temperature annealing at 500 °C or through a contact-firing step at a set-peak temperature of 820 °C in an industrial conveyor-belt furnace, as used in today's commercial solar cell production.

Transition metal oxide contacts, such as molybdenum oxide (MoO<sub>x</sub>), tungsten oxide (WO<sub>x</sub>), and vanadium oxide (VO<sub>x</sub>) have been successfully applied as hole-selective contacts to c-Si.<sup>[1–3]</sup> In contrast, there are few well-tested materials applicable as electron-selective contact layers. From the transition metal oxides, titanium oxide (TiO<sub>x</sub>), tantalum oxide (TaO<sub>x</sub>), and magnesium oxide (MgO<sub>x</sub>) are known as possible candidates for electron-selective materials.<sup>[4–6]</sup> In addition, also nitrides, such as TiN have also been demonstrated to be applicable as electron-selective contact materials.<sup>[7]</sup> The best silicon solar cells featuring an electron-selective contact based on TiO<sub>x</sub> have been achieved so far with TiO<sub>x</sub> layers deposited by thermal atomic layer deposition (ALD), covered by aluminum (Al).<sup>[4,8–10]</sup> In 2016, an efficiency of

## 1. Introduction

Novel carrier-selective contacts based on nonsilicon-based materials might have the potential to replace the classical high-temperature diffused emitters in future high-efficiency silicon solar cells. There is an extraordinary diversity of materials, which are in principle applicable as hole- or electron-selective contacts on crystalline silicon (c-Si). Much research has already been devoted to the field of alternative hole-selective contacts.


21.6% was demonstrated by Yang et al. on a c-Si solar cell featuring a full-area SiO<sub>y</sub>/TiO<sub>x</sub>/Al rear contact.<sup>[4]</sup> Featuring a full-area rear metallization by thermal evaporation of a few nanometer thin Al and a 2 μm-thick Ag layer on the ALD-TiO<sub>x</sub>, this solar cell demonstrated the promising potential of ALD-TiO<sub>x</sub> as electron-selective layer on c-Si solar cells. The outstandingly low contact resistivity  $\rho_c$  achieved by Yang et al. of  $\approx 20 \text{ m}\Omega \text{ cm}^2$  was achieved by a 2.5 nm-thick TiO<sub>x</sub> layer.<sup>[4]</sup> The value of  $\rho_c$  increased strongly with increasing TiO<sub>x</sub> thickness, showing a  $\rho_c$  value of  $\approx 200 \text{ m}\Omega \text{ cm}^2$  measured for a 5.5 nm-thick TiO<sub>x</sub> layer. Note that only 1 year later, the same authors achieved an efficiency of 22.1% by further optimization.<sup>[8]</sup> Allen et al. demonstrated that when using Ca as an overlying metal and implementing TiO<sub>x</sub>/Ca/Al contacts into n-type silicon solar cells as a local rear contact with a contact fraction of  $\approx 6\%$ , a further reduction in  $\rho_c$  to  $\approx 5 \text{ m}\Omega \text{ cm}^2$  was achieved, enabling an efficiency of 21.8%.<sup>[10]</sup> In 2018, a TiO<sub>x</sub>/LiF<sub>x</sub>/Al contact stack was introduced as a rear electron-selective contact to c-Si solar cells. By applying this stack to just around 1% of the rear of an n-type silicon solar cell, a record conversion efficiency of 23.1% and an open-circuit voltage of 695 mV were demonstrated for c-Si solar cells with TiO<sub>x</sub>-based electron-selective rear contacts, so far the best cell results achieved including TiO<sub>x</sub>-based selective contacts.<sup>[11]</sup>

Nevertheless, all cell designs published so far feature TiO<sub>x</sub> contacts on a planar cell rear that was fully covered by Al. The evaluation of the efficiency potential of TiO<sub>x</sub>-based contacts has previously been based on experimental data of the surface recombination velocity demonstrated by Yang et al., which were, however, measured on non-metallized silicon lifetime samples.<sup>[8,12]</sup> The impact of metallization on the efficiency potential

Dr. V. Titova, Prof. J. Schmidt  
Photovoltaics Department  
Institute for Solar Energy Research Hamelin (ISFH)  
Am Ohrberg 1, 31860 Emmerthal, Germany  
E-mail: titova@isfh.de

Prof. J. Schmidt  
Institute of Solid-State Physics  
Leibniz University Hannover  
Appelstr. 2, 30167 Hannover, Germany

Dr. V. Titova  
Gottfried Wilhelm Leibniz Universität Hannover

 The ORCID identification number(s) for the author(s) of this article can be found under <https://doi.org/10.1002/pssr.202100246>.

© 2021 The Authors. physica status solidi (RRL) Rapid Research Letters published by Wiley-VCH GmbH. This is an open access article under the terms of the Creative Commons Attribution-NonCommercial-NoDerivs License, which permits use and distribution in any medium, provided the original work is properly cited, the use is non-commercial and no modifications or adaptations are made.

DOI: 10.1002/pssr.202100246

has therefore not been taken into account so far. The aim of this study is to determine the efficiency potential of  $\text{TiO}_x$ -based electron-selective contacts including the effects of metallization. We experimentally determine the selectivity parameter  $S_{10} = \log_{10}(V_{\text{th}}/J_0\rho_c)$  ( $V_{\text{th}}$  being the thermal voltage) from the measured recombination current density parameter  $J_0$  and the contact resistance  $\rho_c$ , both measured on Al-metallized silicon samples.<sup>[13]</sup> We also examine the impact of different annealing procedures, including an industrial-type fast-firing step performed in an infrared conveyor-belt furnace, as it is routinely used in the industrial silicon solar cell production today. The highest achieved selectivity is shown to be compatible with an industrial firing step, making  $\text{TiO}_x$  relevant to industrial solar cells.

## 2. Experimental Section

### 2.1. Measurement Methods

To assess the passivation quality of passivating contact layers on silicon, in previous studies mainly unmetallized samples were characterized, because the traditionally used photoconductance-based measurement techniques use inductive coupling to a resonant circuit and any metal within the coil detection area is leading to detection problems.<sup>[12,14]</sup> As the metallization might have a quite significant impact on the passivation quality, in this study, we have chosen another measurement approach.

To measure injection-dependent carrier lifetimes on fully one-side-metallized silicon samples, we applied the dynamic infrared lifetime mapping (dyn-ILM) method.<sup>[15]</sup> This method uses the proportionality of the sub-bandgap infrared light (IR) emission of the silicon sample and the number of free charge carriers in the sample.<sup>[16]</sup> **Figure 1** shows a schematic of our in-house developed infrared lifetime mapping (ILM) measurement setup.<sup>[15,16]</sup> The sample is placed on a temperature-controlled gold mirror, which is heated to  $\approx 70^\circ\text{C}$ . Due to the elevated temperature, the free carrier emission is increased and, thus, the signal-to-noise ratio is improved. The sample is illuminated by three light emitting diode (LED) arrays that emit photons with a wavelength of 930 nm, exciting electron-hole pairs in the silicon sample. An infrared camera (SC6800, FLIR Systems) placed above the sample records the

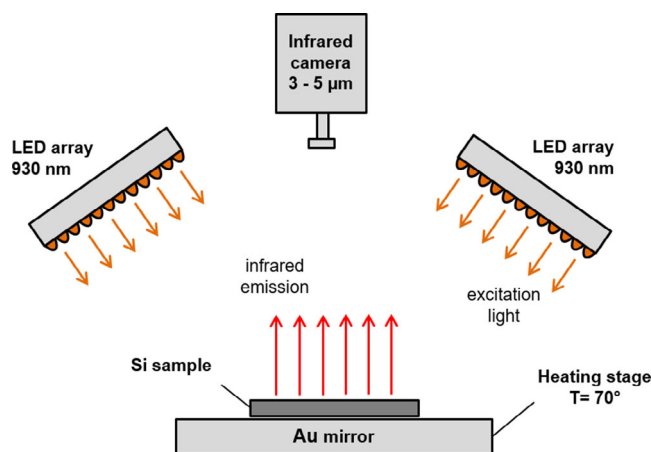


**Figure 1.** Infrared lifetime mapping (ILM) set-up used to extract  $J_0$  on c-Si samples with  $\text{TiO}_x/\text{Al}$  layers at the rear.

infrared emission in a wavelength range between 3 and 5  $\mu\text{m}$ . The use of an IR camera allows to perform spatially resolved carrier lifetime measurements. From the time-dependent measurement of the emitted IR photons, the effective lifetime  $\tau_{\text{eff}}$  is determined, as described in detail by Ramspeck et al.<sup>[16]</sup> Due to the fact that we use a dynamic approach, lateral variations in the optics of the sample have no impact on the measured effective lifetime.

An advantage of the dyn-ILM compared with photoconductance-based lifetime measurements based on coupling the silicon sample to the coil of a resonant circuit is that it is also applicable to silicon samples, which are metallized on the rear. This is of great benefit to determine the impact of the aluminum metallization in the c-Si/ $\text{SiO}_y/\text{TiO}_x/\text{Al}$  stack. In this study, we fabricate silicon lifetime samples (see **Figure 2a**) where half of the rear surface is metallized with Al. As the camera-based dyn-ILM gives a spatially resolved lifetime image with no direct impact of the laterally varying sample optics, it is though possible to have a direct comparison between metallized and non-metallized surface passivation behavior.

For the characterization of the contact resistivity of c-Si/ $\text{TiO}_x$  contacts, the Cox and Strack approach is applied.<sup>[17]</sup> This method is based on a series of circular metal contact areas on the semiconductor, with a range of diameters. Contacting by means of a contact needle, current flows from an upper circular ohmic contact area of diameter  $d$ , through a semiconductor of thickness  $W$ , into a metallized rear contact, which connects the entire sample. For each single front contact, the current-voltage characteristic in the dark is measured using an  $I$ - $V$  tester (LOANA System, pv tools, Hamelin, Germany) at a temperature of  $25^\circ\text{C}$ . From the  $I$ - $V$  measurements, the contact resistivity  $\rho_c$  is calculated, whereby the  $\rho_c$  values are obtained by fitting the resistivity versus the reciprocal contact area  $A$ .

### 2.2. Sample Preparation

For the  $J_0$  measurements, we used n-type Cz-Si wafers with resistivities between 1.4 and 1.5  $\Omega\text{cm}$  and a wafer thickness of 300  $\mu\text{m}$ . **Figure 2a** shows a schematic of the cross section of a lifetime sample.

The lifetime samples characterized by dynamic ILM measurements were not symmetrically passivated on both surfaces. Due to the illumination of the front side, only the rear side of the sample was metallized. A single silicon nitride ( $\text{SiN}_2$ ) passivation layer with a refractive index of  $n = 2.4$  and a thickness of 70 nm was deposited using plasma-enhanced chemical vapor deposition (PECVD; Plasmalab 80+, Oxford Instruments) on the front side. On the rear side, a  $\text{SiO}_y/\text{TiO}_x$  stack, containing a natively grown  $\text{SiO}_y$  layer ( $\approx 1.3$  nm thick) and a 3 nm-thick  $\text{TiO}_x$  layer were deposited. To grow the ultrathin native  $\text{SiO}_y$  prior to the  $\text{TiO}_x$  deposition, the samples were stored in ambient environment for 3 months after RCA cleaning (RCA = Radio Corporation of America).

To examine the impact of aluminum on the surface passivation quality, only half of the sample was metallized by 1  $\mu\text{m}$  of aluminum through a shadow mask using e-beam evaporation. With this half-metallized geometry of the sample rear, it was possible to have a direct comparison between metallized and non-metallized surface passivation behavior.

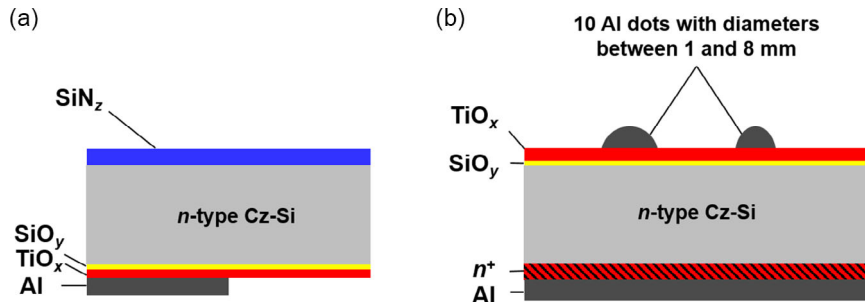


**Figure 2.** a,b) Schematics of cross sections of a) a lifetime sample used to determine the recombination current density parameter  $J_0$  using the dynamic ILM method and b) the sample structure used to extract the contact resistivity  $\rho_c$ .

From the measured lifetime  $\tau_s$ , which we assume here to be surface limited, the recombination current density prefactor  $J_0$  of the total sample, including front and rear recombination, is extracted. On a reference sample, which was symmetrically passivated with  $\text{SiN}_z$ , we extracted the recombination current density prefactor of the front side  $J_{0,\text{front}}$  to be  $9 \text{ fA cm}^{-2}$ . As the dyn-ILM lifetime measurements were carried out under low-injection conditions, the recombination current density prefactor at the sample rear can now be calculated using the Equation (1)

$$J_{0,\text{rear}} = \frac{n_i^2 q W}{\tau_s N_{\text{dop}}} - J_{0,\text{front}} \quad (1)$$

where  $n_i$  is the intrinsic carrier concentration of silicon,  $q$  is the elementary charge,  $W$  is the sample thickness, and  $N_{\text{dop}}$  is the doping concentration of the silicon wafer.

We used the same n-type Cz-Si silicon wafers for the measurements of the contact resistivity  $\rho_c$ . The cross section of our Cox and Strack samples is shown in Figure 2b. On the front side of the samples,  $\text{TiO}_x$  layers with thicknesses of 2 and 5 nm were deposited. Ten dot-shaped Al contacts of  $1 \mu\text{m}$  thickness with different diameters, ranging from 1 to 8 mm, were electron-beam-evaporated on top through a nickel shadow mask (BAK 550, Oerlikon Balzers AG). To obtain an ohmic contact on the rear side, an  $n^+$ -layer ( $80 \Omega \text{ sq}^{-1}$ ) was formed by phosphorus diffusion in a quartz-tube furnace (HT 2000, Centrotherm) at a temperature of  $855^\circ\text{C}$  using a liquid  $\text{POCl}_3$  source. On top of the  $n^+$ -layer, a  $1 \mu\text{m}$ -thick Al film was evaporated.

### 3. Experimental Results

#### 3.1. Contact Resistivity Measurements

**Figure 3** shows the measured current of Al-metallized  $\text{SiO}_y/\text{TiO}_x$  stacks on n-type c-Si as a function of voltage in the as-deposited (blue line) and annealed states (red lines). All  $I$ - $V$  curves shown have been measured for the largest contact diameter (8 mm) of the Cox and Strack test structures. Annealing was carried out on a hot-plate in ambient environment at a temperature of  $250^\circ\text{C}$  for 10 min for samples with 2 nm-thick  $\text{TiO}_x$  (red dashed line). Annealing at a higher temperature of  $500^\circ\text{C}$  for 1 min was carried out on the contact resistivity sample with slightly thicker  $\text{TiO}_x$  layers of 3 nm and is included in Figure 3 as a dark red

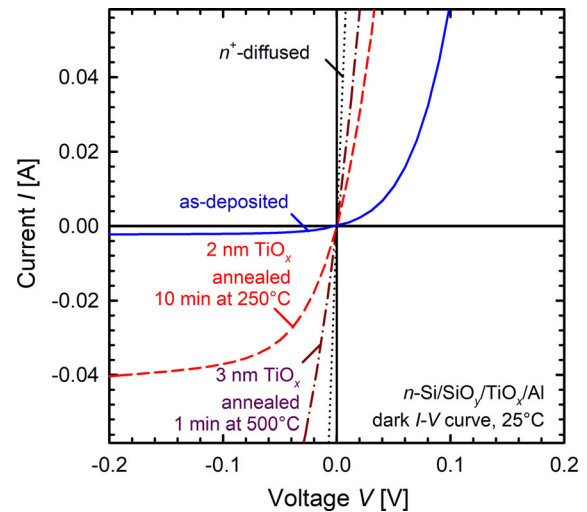


**Figure 3.** Current–voltage measurements of contact resistivity test structures showing rectifying behavior of the n-Si/ $\text{SiO}_y/\text{TiO}_x/\text{Al}$  contact (circular Al contact with 8 mm diameter) directly after deposition and ohmic behavior after annealing.

dashed line. The  $I$ - $V$  data from a reference sample with phosphorus-diffused front and rear ( $80 \Omega \text{ sq}^{-1}$ ) are also shown in the Figure 3 as a black dotted line.

Compared with the reference  $n^+$ -diffused sample, the n-Si/ $\text{SiO}_y/\text{TiO}_x/\text{Al}$  contacts exhibit nonohmic, rectifying (Schottky) behavior directly after deposition, shown in Figure 3 by the blue solid line.

The measurement results are evaluated at a current density of  $40 \text{ mA cm}^{-2}$ , which approximately corresponds to the maximum current density of a solar cell. Comparing the as-deposited and annealed states, it can be observed that after a short annealing the  $\text{TiO}_x$ -based contact exhibits a more pronounced ohmic  $I$ - $V$  behavior, especially in the first quadrant. If a higher annealing temperature is applied, the  $I$ - $V$  curve becomes even more ohmic and similar to that of the reference sample. This allows an accurate extraction of  $\rho_c$  in the evaluation range. The extracted  $\rho_c$  values for the contact structures before and after annealing are shown in **Figure 4** and **5**.

**Figure 4** shows the measured contact resistivity  $\rho_c$  of Al-metallized  $\text{SiO}_y/\text{TiO}_x$  stacks on n-type c-Si as a function of the  $\text{TiO}_x$  film thickness in the as-deposited (blue triangles)

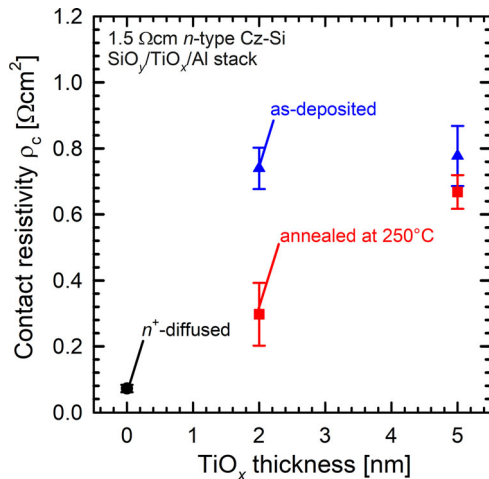


**Figure 4.** Contact resistivities  $\rho_c$  as a function of the  $\text{TiO}_x$  film thickness in the as-deposited (blue triangles) and the annealed (250 °C, 10 min) states (red squares). Also shown is a reference sample with a front and rear side  $n^+$ -layer.

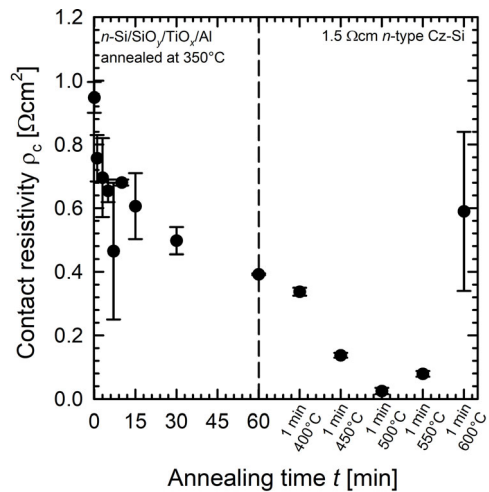


**Figure 5.** Contact resistivity  $\rho_c$  of a  $\text{SiO}_y/\text{TiO}_x/\text{Al}$  stack as a function of annealing time  $t$ . On the left side from the dashed line, the annealing period at a temperature of 350 °C on a hot-plate is plotted. On the right side, the annealing temperature applied to the samples was increased in 50 °C steps up to 600 °C, with a constant annealing time of 1 min.

and annealed states (red squares). Annealing was carried out on a hot-plate at a temperature of 250 °C for 10 min. All  $\rho_c$  values in the plot represent the average over two samples. Two reference samples (black circles) are included, where front and rear sides are phosphorus-diffused ( $80 \Omega \text{sq}^{-1}$ ) and metallized with 1  $\mu\text{m}$ -thick Al layers.

For 5 nm-thick  $\text{TiO}_x$ , a  $\rho_c$  value of  $(0.78 \pm 0.09) \Omega \text{cm}^2$  is measured before annealing and  $(0.67 \pm 0.05) \Omega \text{cm}^2$  after annealing. For  $\text{TiO}_x$  layers with a thickness of 2 nm, a value of  $(0.74 \pm 0.06) \Omega \text{cm}^2$  is measured before annealing, which improves to  $(0.3 \pm 0.1) \Omega \text{cm}^2$  after the 10 min anneal at 250 °C. It can, therefore, be concluded that  $\text{TiO}_x$  layers with

interfacial oxide enable a low contact resistivity ( $<0.5 \Omega \text{cm}^2$ ) after annealing at 250 °C, provided that they are sufficiently thin.

To investigate the impact of higher annealing temperatures on the contact resistivity, the annealing temperature was varied. A prolonged annealing at 350 °C up to 60 min was applied, followed by a subsequent stepwise increase in the annealing temperature in 50 °C steps up to 600 °C. We observe that the contact resistivity of the  $\text{SiO}_y/\text{TiO}_x/\text{Al}$  contact on n-type silicon decreases with increasing annealing time, as shown in Figure 5. After a 60 min anneal at 350 °C, we measure a contact resistivity of  $0.4 \Omega \text{cm}^2$ . Afterward, the samples are annealed for an additional 1 min with increasing temperature starting at 400 °C. The lowest contact resistivity of  $(0.025 \pm 0.01) \Omega \text{cm}^2$  is obtained after annealing at 500 °C. Higher temperatures lead to an increase in the  $\rho_c$  value. We conjecture that the increase in  $\rho_c$  at higher annealing temperatures might be caused by the crystallization of the  $\text{TiO}_x$ , but it would require further detailed studies to check this hypothesis.

To verify that a low contact resistivity can be achieved in only one annealing step,  $\text{SiO}_y/\text{TiO}_x/\text{Al}$  test samples were annealed directly at 500 °C for 1 min. The initially high contact resistivity of  $(0.95 \pm 0.05) \Omega \text{cm}^2$  was drastically reduced after an 1 min anneal at 500 °C to a very low  $\rho_c$  value of  $(0.06 \pm 0.003) \Omega \text{cm}^2$ , which is among the lowest  $\rho_c$  values reported for  $\text{TiO}_x$ -based contacts in the literature.

To further reduce the annealing period and to examine whether  $\text{TiO}_x$ -based contacts are compatible with the industrial production of solar cells, we also applied a firing step in an industrial infrared belt furnace (DO-FF-8.600-300, Centrotherm). The firing furnace consists of six heating zones and the firing is carried out in ambient environment, whereas maintaining the set-temperature defined for each zone. Different heating and cooling rates are realized by varying the peak temperature of each zone as well as the belt speed. We record the temperature profile using a DATAPAQ Insight Oven Tracker to properly correlate the temperature profile, which the samples were exposed to with the measured results. To record the temperature profile, a temperature probe is attached to a sample processed identically to the sample under investigation. **Figure 6** shows two temperature profiles measured on samples with a  $\text{SiO}_y/\text{TiO}_x/\text{Al}$  stack.

The first firing step applied to the sample features a set-peak temperature  $\vartheta_{\text{peak}}$  of 820 °C and a belt speed  $v_{\text{belt}}$  of  $6.8 \text{ m min}^{-1}$ . The corresponding temperature profile is shown as dashed black curve in Figure 6. The second settings (red solid line in Figure 6) represent a set-peak temperature  $\vartheta_{\text{peak}}$  of 750 °C and a belt speed  $v_{\text{belt}}$  of  $5.3 \text{ m min}^{-1}$ . These firing conditions are typical for industrial screen-printed silicon solar cells.

We define the firing duration as the period during which the samples have been at a temperature exceeding 500 °C. For the first oven setting (indicated as black dashed line in Figure 6), the sample is exposed to a temperature of  $>500 \text{ °C}$  for 3.4 s with a highest measured peak temperature of 550 °C. For these firing conditions, a contact resistivity  $\rho_c$  of  $0.25 \Omega \text{cm}^2$  was measured on a fired sample. For the second firing conditions (red solid line in Figure 6), the sample moves slower through the furnace with a belt speed of  $5.3 \text{ m min}^{-1}$ . To avoid the exposition of the sample to temperatures  $>550 \text{ °C}$  for a longer period, the set-peak temperature is reduced to 750 °C. In addition, the peak temperature of zone three is increased from 500 to 650 °C. This helps to

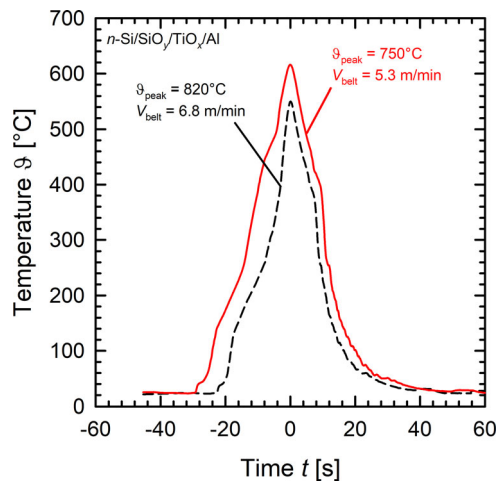


**Figure 6.** Temperature profiles measured on a silicon sample with  $\text{SiO}_x/\text{TiO}_x/\text{Al}$  stack during firing using the DATAPAQ Insight Oven Tracker. The profiles for two firing conditions (set conditions) are displayed. The red solid curve corresponds to a set-peak temperature  $\vartheta_{\text{peak}}$  of  $750^\circ\text{C}$  and a belt speed of  $v_{\text{belt}}$  of  $5.3\text{ m min}^{-1}$ . The black dashed curve represents  $\vartheta_{\text{peak}}$  of  $820^\circ\text{C}$  and  $v_{\text{belt}}$  of  $6.8\text{ m min}^{-1}$ .

increase the temperature more gently. With the second firing conditions (red solid line in Figure 6) a measured peak temperature of  $616^\circ\text{C}$  is reached and the sample is exposed to a temperature  $>500^\circ\text{C}$  for almost 9 s. In this case, a significantly reduced contact resistivity  $\rho_c$  of  $0.05\ \Omega\text{ cm}^2$  was achieved after firing.

In Table 1, the contact resistivities after firing and after hot-plate annealing at  $500^\circ\text{C}$  for 1 min are compared. Our measurements clearly demonstrate that a short firing step in an industrial conveyor-belt furnace is capable of replacing the hot-plate annealing step to obtain low contact resistivities based on n-Si/ $\text{SiO}_x/\text{TiO}_x/\text{Al}$  electron-selective contacts.

### 3.2. $J_0$ Measurements of n-Si/ $\text{SiO}_x/\text{TiO}_x/\text{Al}$ Contacts

The lowest  $\rho_c$  values achieved in this work have been reached by hot-plate annealing at  $500^\circ\text{C}$  as well as by firing using an industrial conveyor-belt furnace. To be able to estimate the selectivity  $S_{10}$  for these cases, we carried out dyn-ILM measurements for these post-treatment conditions on half-metallized samples to measure the associated  $J_0$  values.

**Table 1.** Contact resistivity  $\rho_c$  after annealing at  $500^\circ\text{C}$  and firing in an industrial conveyor-belt furnace.

Postdeposition treatment	Duration at a temperature $>500^\circ\text{C}$ [s]	Measured peak temperature $[\text{C}]$	Measured contact resistivity $\rho_c$ [ $\Omega\text{ cm}^2$ ]
Hot-plate annealing	60	500	0.06
Belt-furnace firing $\vartheta_{\text{peak}} = 820^\circ\text{C}$ , $v_{\text{belt}} = 6.8\text{ m min}^{-1}$	3.4	550	0.25
Belt-furnace firing $\vartheta_{\text{peak}} = 750^\circ\text{C}$ , $v_{\text{belt}} = 5.3\text{ m min}^{-1}$	8.6	616	0.05

Figure 7a shows a dyn-ILM image of a lifetime sample annealed at  $350^\circ\text{C}$  for 7 min. It is obvious that the annealed  $\text{SiO}_x/\text{TiO}_x$  stacks show a clear difference in surface passivation quality on n-type c-Si between the Al-metallized and nonmetallized areas.

As shown in Figure 7a, the effective lifetime  $\tau_{\text{eff}}$  on the non-metallized area has already reached its maximum of 2 ms (at  $\Delta n = 1 \times 10^{15}\text{ cm}^{-3}$ ) after a short anneal of only 1 min. The lifetime on the metallized area is still modest and hardly exceeds 0.4 ms even after prolonged annealing. The metallized area represents a potential solar cell, as the rear side of the solar cell is covered by aluminum. Therefore, only the  $J_0$  values of the metallized area will be considered later for the selectivity evaluation.

Figure 8a shows the measured effective lifetime  $\tau_{\text{eff}}$  and Figure 8b shows the recombination current density parameter  $J_0$  ( $J_{0,\text{rear}}$  in Equation (1)), respectively, for samples with 3 nm-thick  $\text{TiO}_x$  layers at various annealing durations. The symbols shown in Figure 8a correspond to the data interpolated to an injection density of  $\Delta n = 10^{15}\text{ cm}^{-3}$  from the injection-dependent lifetime measurements carried out using dyn-ILM method.

For  $\text{TiO}_x$  layers with a thickness of 3 nm, a short anneal at  $350^\circ\text{C}$  is sufficient to significantly improve the surface passivation quality of Al-metallized samples. Directly after Al evaporation, a very high  $J_0$  value of  $1726\text{ fA cm}^{-2}$  is measured, which significantly improves to a value of  $242\text{ fA cm}^{-2}$  after annealing for 15 min. Figure 8c shows the measured contact resistivity  $\rho_c$  as a function of annealing time. A  $\rho_c$  value of  $0.95\ \Omega\text{ cm}^2$  is measured directly after Al evaporation, however, this value improves after a 7 min anneal at  $350^\circ\text{C}$  to  $(0.47 \pm 0.22)\ \Omega\text{ cm}^2$ .

Figure 7b shows a dyn-ILM lifetime image of a sample annealed at  $500^\circ\text{C}$  for 1 min. The 1 min anneal at  $500^\circ\text{C}$  results in a positive impact on the passivation quality. Nevertheless, the  $J_0$  values are slightly higher in comparison with the values achieved after an annealing at  $350^\circ\text{C}$ . However, the samples show an improvement from  $1735$  to  $1327\text{ fA cm}^{-2}$  on the metallized area and  $600$ – $350\text{ fA cm}^{-2}$  on the non-metallized area due to the  $500^\circ\text{C}$  annealing step.

### 3.3. Selectivities $S_{10}$ of $\text{SiO}_x/\text{TiO}_x/\text{Al}$ Contacts

We can now determine the selectivity parameter, defined as  $S_{10} = \log_{10}(V_{\text{th}}/J_0\rho_c)$  ( $V_{\text{th}}$  being the thermal voltage), from the measured  $J_0$  and  $\rho_c$  values.<sup>[13]</sup> Figure 8d clearly shows that the selectivity increases due to the hot-plate annealing at  $350^\circ\text{C}$ . Applying the firing conditions of  $\vartheta_{\text{peak}} = 820^\circ\text{C}$  and  $v_{\text{belt}} = 6.8\text{ m min}^{-1}$ , a  $J_0$  value of  $(271 \pm 54)\text{ fA cm}^{-2}$  was measured for an Al-metallized  $\text{TiO}_x$  contact. Under the same conditions, a relatively large contact resistivity of  $\rho_c = 0.25\ \Omega\text{ cm}^2$  was extracted. Combining the measured  $J_0$  and  $\rho_c$  values, we determine a corresponding selectivity  $S_{10}$  of 11.6. Using the relation between maximum achievable efficiency  $\eta_{\text{max}}$  and the selectivity parameter  $S_{10}$  according to Brendel et al., the extracted value of  $S_{10} = 11.6$  corresponds to a maximum efficiency  $\eta_{\text{max}}$  of 24.1%.<sup>[18]</sup> Applying the second set of firing conditions  $\vartheta_{\text{peak}} = 750^\circ\text{C}$  and  $v_{\text{belt}} = 5.3\text{ m min}^{-1}$ , a degradation of  $J_0$  from  $1453$  to  $1853\text{ fA cm}^{-2}$  on the metallized area and from  $548$  to  $795\text{ fA cm}^{-2}$  on the non-metallized area is observed, respectively.

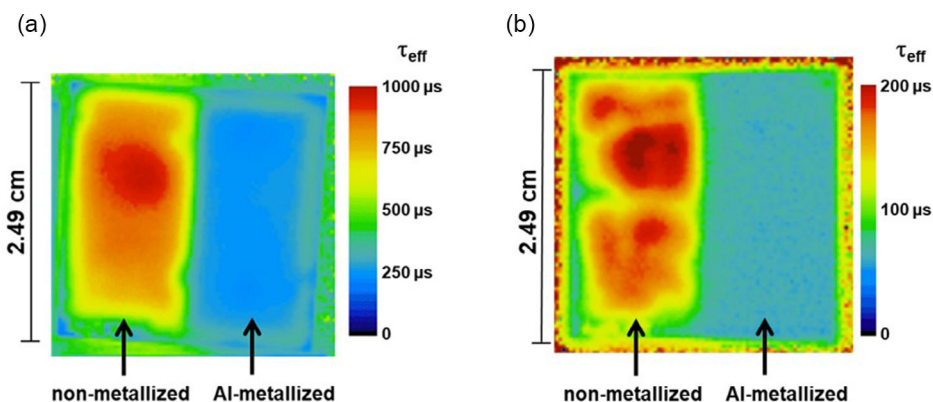


**Figure 7.** Measured spatially resolved effective lifetime  $\tau_{\text{eff}}$  images from dyn-ILM measurements at a photon flux equivalent to 0.3 suns of 1.5  $\Omega$  cm  $n$ -type Cz-Si samples with  $\text{SiO}_y/\text{TiO}_x$  stacks without metallization on the left and fully metallized by an Al layer on the right. The front sample surface is passivated by  $\text{SiN}_z$ . The samples are annealed at: a) 350  $^\circ\text{C}$  for 7 min and b) 500  $^\circ\text{C}$  for 1 min.

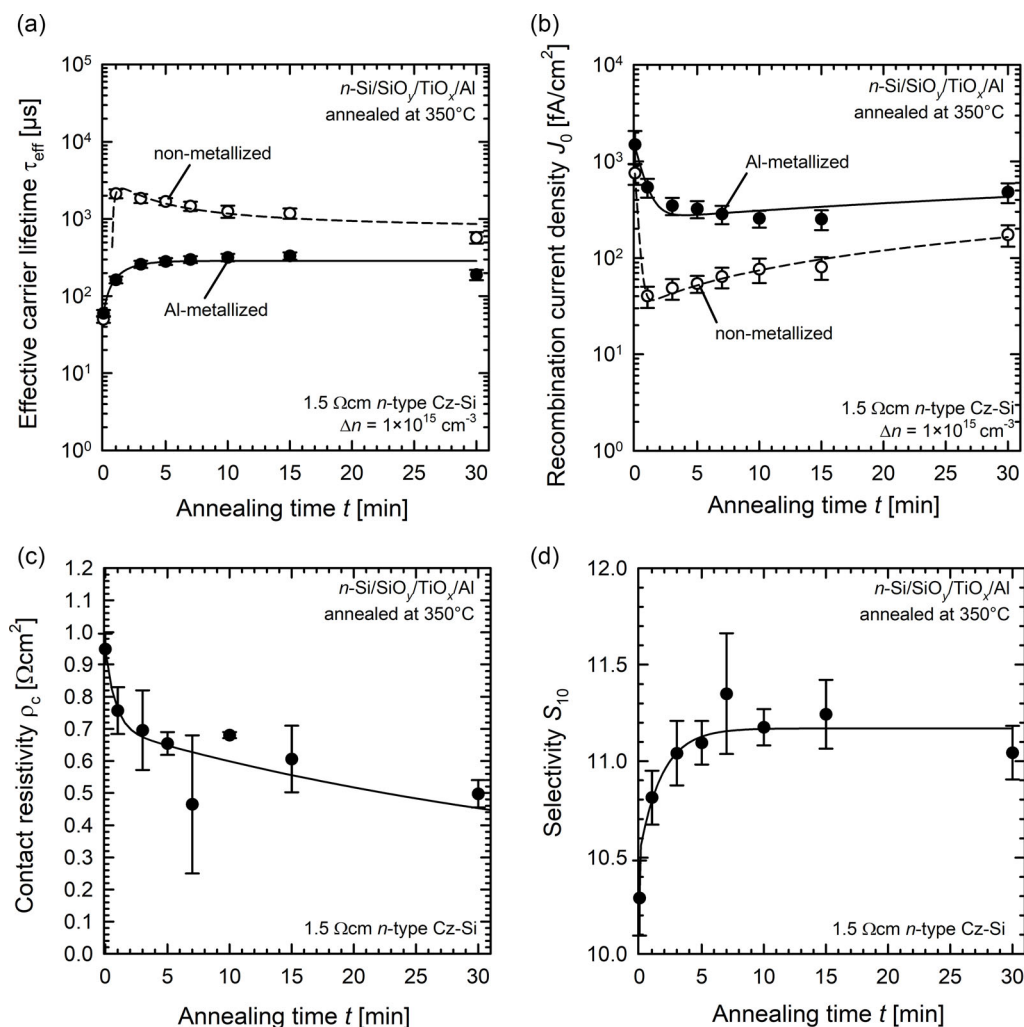


**Figure 8.** a) Measured effective lifetime  $\tau_{\text{eff}}$  at  $\Delta n = 10^{15} \text{ cm}^{-3}$ , b) recombination current density parameter  $J_0$ , c) contact resistivity  $\rho_c$ , and d) calculated selectivity  $S_{10}$  of  $n\text{-Si/SiO}_y/\text{TiO}_x/\text{Al}$  contacts as a function of annealing time  $t$ . Post-deposition annealing treatment is carried out on a hot-plate at 350  $^\circ\text{C}$ .

**Table 2.** Measured  $\rho_c$  and  $J_0$  values together with the resulting selectivity parameter  $S_{10}$ , the optimal contact fraction  $f_{max}$  and the maximum achievable efficiencies  $\eta_{max}$  for Al-metallized samples with 3 nm-thick  $TiO_x$  layers. Lifetime samples and contact resistivity samples have been annealed under the same conditions.

Post-deposition treatment		$\rho_c$ [ $\Omega\text{ cm}^2$ ]	$J_0$ [ $\text{fA cm}^{-2}$ ]	$S_{10}$	$f_{max}$	$\eta_{max}$ [%]
Hot-plate annealing	350 °C, 7 min	$0.47 \pm 0.22$	$285 \pm 81$	$11.3 \pm 0.3$	$0.75 \pm 0.5$	$23.4 \pm 0.8$
	500 °C, 1 min	0.06	$1255 \pm 338$	$11.6 \pm 0.1$	0.09	$24.1 \pm 0.3$
Belt-furnace firing	$820\text{ °C, }6.8\text{ m min}^{-1}$	0.25	$271 \pm 54$	11.6	0.41	24.1
	$750\text{ °C, }5.3\text{ m min}^{-1}$	0.05	$1853 \pm 371$	11.4	0.08	23.8

However,  $\rho_c$  improves significantly during firing to a value of  $0.05\ \Omega\text{ cm}^2$ .

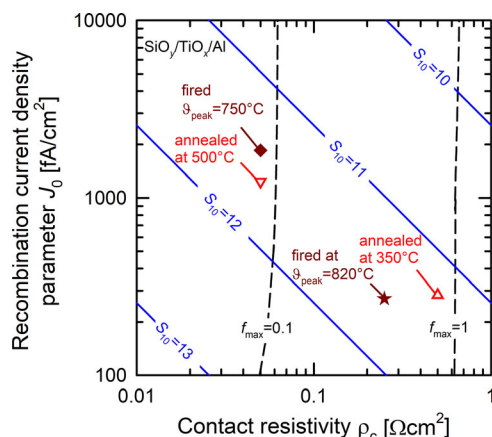
Table 2 shows the measured  $J_0$  and  $\rho_c$  values together with the resulting selectivity parameter  $S_{10}$  and the maximum achievable efficiencies  $\eta_{max}$  of the metallized  $TiO_x$ -based contacts for different postdeposition treatments. Also included is the contacting area  $f_{max}$  maximizing the efficiency, where the noncontacted area is assumed to be perfectly passivated.<sup>[18]</sup>

Figure 9 compiles the best selectivities  $S_{10}$  for  $SiO_y/TiO_x/Al$  stacks achieved in this work. For the electron-selective Al-metallized contact based on 3 nm ALD- $TiO_x$  layers and an ultrathin interlayer of natively grown  $SiO_y$  ( $\approx 1.3$  nm), we demonstrate good selectivities in the range between 11.3 and 11.6. The two data pairs featuring recombination current density parameters  $J_0 > 1000\ \text{fA cm}^{-2}$  demonstrate the lowest contact resistivities of only  $0.05\ \Omega\text{ cm}^2$ . For the annealing conditions with lower temperature or increased belt speed of  $6.8\ \text{m min}^{-1}$  during firing at a set-peak temperature of  $820\text{ °C}$ , we measure significantly higher contact resistivity values of  $0.2\text{--}0.5\ \Omega\text{ cm}^2$ . In contrast, these gentle postdeposition treatment conditions enable a significantly better surface passivation quality, featuring  $J_0$  values of  $\approx 300\ \text{fA cm}^{-2}$ . Note that the different annealing conditions lead

to quite different optimal contact fractions  $f_{max}$  and hence different required cell structures. The conditions leading to low  $\rho_c$  values of  $0.05\ \Omega\text{ cm}^2$ , but large  $J_0$  values  $> 1000\ \text{fA cm}^{-2}$  make local contacts with a contact fraction of 8–9% necessary for optimum efficiencies, whereas the two conditions leading to better surface passivation but increased contact resistivities are suitable for full-area-contacted cells. The obtained selectivities  $S_{10}$  are below values reported for a-Si/c-Si heterojunctions and poly-Si-based passivating contacts, however, they are on a par with selective phosphorus-diffused emitters of state-of-the-art commercial silicon solar cells.<sup>[12]</sup>

#### 4. Conclusions

We have shown that ultrathin ALD- $TiO_x$  films provide not only good passivation of crystalline silicon surfaces, but also provide low contact resistivities  $\rho_c$  on n-type silicon in combination with Al as contact metal. A  $\rho_c$  value of only  $0.06\ \Omega\text{ cm}^2$  was achieved after an annealing step at  $500\text{ °C}$  for 1 min on a hot-plate. By firing in an industrial belt furnace with a temperature of  $\approx 500\text{ °C}$  for  $\approx 9$  s, an even lower  $\rho_c$  value of  $0.05\ \Omega\text{ cm}^2$  was measured. The passivation quality provided by the ultrathin  $TiO_x$  layers was shown to be different for Al-metallized and non-metallized surfaces, which was demonstrated on half-metallized samples, allowing the  $J_0$  extraction of non-metallized and Al-metallized samples using dynamic ILM measurements. The minimum  $J_0$  value on the non-metallized samples was  $41\ \text{fA cm}^{-2}$  after annealing at  $350\text{ °C}$  for 1 min, whereas the minimum  $J_0$  of the Al-metallized area was  $253\ \text{fA cm}^{-2}$  after annealing at  $350\text{ °C}$  for 15 min. Under these annealing conditions, the non-metallized half of the sample showed already a degradation of the passivation quality. For the optimum annealing conditions of the Al-metallized sample, a contact resistivity of  $0.06\ \Omega\text{ cm}^2$  was achieved, leading to a selectivity parameter  $S_{10}$  of  $11.6 \pm 0.1$ . From this extracted  $S_{10}$  value, we were able to extract the maximum achievable efficiency  $\eta_{max}$  of the n-Si/ $SiO_y/TiO_x/Al$  contact to be  $(24.1 \pm 0.3)\%$ . Using a conveyor-belt firing furnace, a contact resistivity of  $0.25\ \Omega\text{ cm}^2$  was reached together with a reasonably low  $J_0$  value of  $(271 \pm 54)\ \text{fA cm}^{-2}$ , leading also to a selectivity  $S_{10}$  of 11.6, and hence, the same maximal achievable efficiency  $\eta_{max}$  of 24.1%, which demonstrates the industrial potential of the novel contacting scheme. Future work might examine ways of further increasing  $S_{10}$ , e.g., by adding Al to the  $TiO_x$  layer. In addition, experiments should be conducted to clarify the physical reason for the parallel improvement of the contact resistivity and the degradation of the surface



**Figure 9.** Recombination current density parameters  $J_0$  and contact resistivities  $\rho_c$  measured on n-Si/ $SiO_y/TiO_x/Al$  contacts annealed under various conditions. The symbols represent the  $(J_0, \rho_c)$  data pairs resulting in the maximum selectivity  $S_{10}$  achieved in this work. The red open triangles correspond to hot-plate annealing at 350 and 500 °C, whereas purple closed symbols correspond to firing in an industrial conveyor-belt furnace under different conditions. Lines of constant selectivity  $S_{10}$  are shown as blue solid lines; lines of constant contact fraction  $f_{max}$  are shown as black dashed lines.

passivation during annealing, which could provide some strategies of further improving the contact properties.

## Acknowledgements

Funding was proved by the German State of Lower Saxony and the German Federal Environmental Foundation (DBU).

Open access funding enabled and organized by Projekt DEAL.

## Conflict of Interest

The authors declare no conflict of interest.

## Data Availability Statement

Research data are not shared.

## Keywords

atomic layer deposition, contact resistivities, electron-selective contacts, selectivities,  $\text{SiO}_y/\text{TiO}_x/\text{Al}$  stacks, titanium oxide

Received: May 5, 2021

Revised: June 11, 2021

Published online: July 11, 2021

- [1] C. Battaglia, S. M. de Nicolás, S. de Wolf, X. Yin, M. Zheng, C. Ballif, A. Javey, *Appl. Phys. Lett.* **2014**, *104*, 113902.  
[2] M. Bivour, J. Temmler, H. Steinkemper, M. Hermle, *Solar Energy Mater. Sol. Cells* **2015**, *142*, 34.

- [3] G. Masmitjà, L. G. Gerling, P. Ortega, J. Puigdollers, I. Martín, C. Voz, R. Alcubilla, *J. Mater. Chem. A* **2017**, *5*, 9182.  
[4] X. Yang, Q. Bi, H. Ali, K. Davis, W. V. Schoenfeld, K. Weber, *Adv. Mater.* **2016**, *28*, 5891.  
[5] Y. Wan, J. Bullock, A. Cuevas, *Sol. Energy Mater. Solar Cells* **2015**, *142*, 42.  
[6] Y. Wan, C. Samundsett, J. Bullock, M. Hettick, T. Allen, D. Yan, J. Peng, Y. Wu, J. Cui, A. Javey, A. Cuevas, *Adv. Energy Mater.* **2017**, *7*, 1601863.  
[7] X. Yang, W. Liu, M. De Bastiani, T. Allen, J. Kang, H. Xu, E. Aydin, L. Xu, Q. Bi, H. Dang, E. AlHabshi, K. Kotsivos, A. AlSaggaf, I. Gereige, Y. Wan, J. Peng, C. Samundsett, A. Cuevas, S. De Wolf, *Joule* **2019**, *3*, 1314.  
[8] X. Yang, K. Weber, Z. Hameiri, S. De Wolf, *Prog. Photovoltaics* **2017**, *25*, 896.  
[9] V. Titova, J. Schmidt, *AIP Adv.* **2018**, *8*, 125023.  
[10] T. G. Allen, J. Bullock, Q. Jeangros, C. Samundsett, Y. Wan, J. Cui, A. Hessler-Wyser, S. De Wolf, A. Javey, A. Cuevas, *Adv. Energy Mater.* **2017**, *7*, 1602606.  
[11] J. Bullock, Y. Wan, M. Hettick, X. Zhaoran, S. P. Phang, D. Yan, H. Wang, W. Ji, C. Samundsett, Z. Hameiri, D. Macdonald, A. Cuevas, A. Javey, *Adv. Energy Mater.* **2019**, *9*, 1803367.  
[12] J. Schmidt, R. Peibst, R. Brendel, *Sol. Energy Mater. Sol. Cells* **2018**, *187*, 39.  
[13] R. Brendel, M. Rienecker, R. Peibst, in *Proc. 32nd European Photovoltaic Solar Energy Conf.*, WIP, Munich, Germany, **2016**, pp. 447–451.  
[14] V. Titova, B. Veith-Wolf, D. Startsev, J. Schmidt, *Energy Procedia* **2017**, *124*, 441.  
[15] K. Ramspeck, S. Reissenweber, J. Schmidt, K. Bothe, R. Brendel, *Appl. Phys. Lett.* **2008**, *93*, 102104.  
[16] K. Ramspeck, K. Bothe, J. Schmidt, R. Brendel, *J. Appl. Phys.* **2009**, *106*, 114506.  
[17] R. H. Cox, H. Strack, *Solid-State Electron.* **1967**, *10*, 1213.  
[18] R. Brendel, R. Peibst, *IEEE J. Photovoltaics* **2016**, *6*, 1413.